

Instabilities in Gravity Driven Flow of Thin Fluid Films*

L. Kondic[†]

Abstract. This paper presents theoretical, computational, and experimental aspects of the instability development in the flow of thin fluid films. The theoretical part involves basic fluid mechanics and presents derivation of the thin film equation using lubrication approximation. A simplified version of this equation is then analyzed analytically using linear stability analysis, and also numerically. The results are then compared directly to experiments. The experimental part outlines the setup, as well as data acquisition and analysis. This immediate comparison to experiments is very useful for gaining better insight into the interpretation of various theoretical and computational results.

Key words. nonlinear partial differential equations, perturbation theory, finite difference methods, fluid dynamics

AMS subject classifications. 76D08, 35G30, 65M06

PII. S0036144502401358

I. Introduction. Most traditional programs in applied mathematics, engineering, or physics include classes such as ordinary and partial differential equations, at least one class in programming and numerical methods, and introductory physics, to name just a few. Very often, however, there is no time for students to develop deeper understanding of some particular problem that would allow them to apply their acquired knowledge. Further, most of the typical classwork is individual, while the skills that are needed in “real-life” surroundings include group work and a significant amount of interaction between the members of a team.

One way to help students bridge the gap between their common classwork and more involved problems, as well as to round off their undergraduate education, is to offer a class that (i) is interdisciplinary, (ii) is related to some problem of practical relevance and/or close to the forefront of current scientific research, and (iii) unifies many different (and often disjoint) aspects of the classes they have already taken. Satisfying all these requirements is not easy. At the same time, formulating an appropriate project is extremely gratifying, since working on a new and not yet completely understood problem provides significant motivation and interest.

The project presented here was carried out at the Department of Mathematical Sciences of NJIT during the Spring 2001 semester. It contains theoretical, computational, and experimental components, and includes some aspects of data analysis and image processing, as well as more classical methods related to ordinary and partial

*Received by the editors January 21, 2002; accepted for publication (in revised form) July 19, 2002; published electronically February 3, 2003. This work was partially supported by NSF grant INT-0122911 and NJIT grant 421210.

<http://www.siam.org/journals/sirev/45-1/40135.html>

[†]Department of Mathematical Sciences and Center for Applied Mathematics and Statistics, New Jersey Institute of Technology, Newark, NJ 07102 (kondic@pattern.njit.edu).

differential equations, such as linear stability and numerical analysis. On the theoretical side it requires an introduction to basic fluid mechanics, and on the experimental one, the building of a (simple) apparatus. Since these different aspects are time consuming, the whole semester was dedicated to a single project. It is possible to modify the problem so that it is completed faster, assuming that the students are familiar with some fluid mechanics and that an experimental setup already exists.

The presentation assumes familiarity with basic ordinary and partial differential equations (ODEs and PDEs), some knowledge of finite difference schemes, and not much more. Depending on the level of a given class, and on the time frame, various aspects of the problem can be included or not. In particular, more advanced topics, such as implicit schemes in Appendix B or similarity solutions in Appendix D, can be omitted if appropriate. In the opposite direction, a number of suggestions for approaching more complex issues (such as numerical solution to the eigenvalue problem, (36), or understanding of its eigenfunctions) have been provided. The addition of some of these topics would make this problem appropriate as a project for graduate students.

On either level, the flow of thin fluid films is very convenient as a class/module. The experiment itself does not require too much space, and it is safe and easy to perform. The results can be obtained with the needed degree of precision using a still picture camera or a camcorder. Finally, instabilities of any sort are always interesting, and this problem is not an exception; the experimental results (see Figure 1) are intriguing and strongly motivate the students and the instructor.

This paper is organized as follows. In section 2, I give an outline of the underlying mathematical model and provide references that are both informative and also appropriate for advanced undergraduate students. Section 3 provides an overview of the experimental setup, as well as of the data collection and analysis. Significant material is contained in the appendices, which include description of the numerical methods, lubrication approximation, an outline of the linear stability analysis, and the self-similar solution. Exercise problems at the ends of the sections often provide more detailed information needed for deriving some of the important equations.

2. Theoretical Modeling. The starting point for modeling flow of thin films are the Navier–Stokes (N–S) equations. These PDEs are essentially an application of Newton’s second law to the flow of fluids; see, e.g., the book by Acheson [2] for a simple derivation and interpretation of various terms. Assuming also incompressibility of the fluid film, which leads to the divergence-free condition

$$(1) \quad \nabla \cdot \mathbf{u} = 0,$$

these equations are as follows:

$$(2) \quad \frac{\partial \mathbf{u}}{\partial t} + (\mathbf{u} \cdot \nabla) \mathbf{u} = -\frac{1}{\rho} \nabla p + \frac{\mu}{\rho} \nabla^2 \mathbf{u} + g \sin \alpha \mathbf{i} - g \cos \alpha \mathbf{k},$$

where \mathbf{u} is the fluid velocity, ρ is the density, and μ is the viscosity, which effectively introduces “friction” into the problem. The last term is due to the normal component of gravity, and the next to last stands for the downhill component. The coordinate frame is as shown in Figure 2. In section 2.3.1 and Appendix D, I discuss two important aspects of the typical fluid profile, namely, the formation of a ridge just behind the front and thinning of the fluid far behind.

The N–S equations are to be coupled with the appropriate initial and boundary conditions (BCs). Initial conditions are relatively simple: one just needs to prescribe

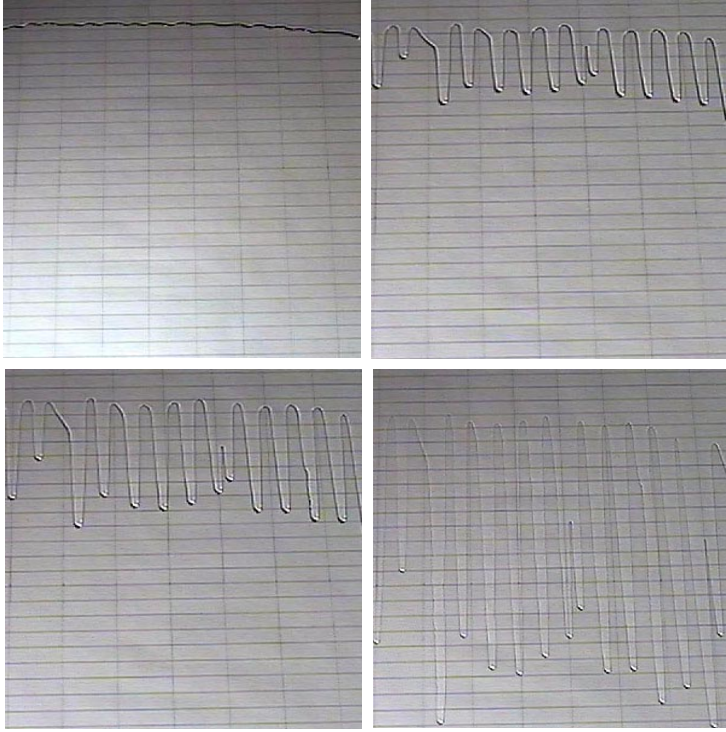


Fig. 1 Photos of the fluid flowing down an inclined plane at times = 0.5, 4, 8, 84 sec after release (increasing from top left to bottom right). The inclination angle is $\alpha = 60^\circ$; other fluid and flow parameters are given in section 3. The distance between the solid lines is 5 cm in the transverse, and 2 cm in the downhill direction.

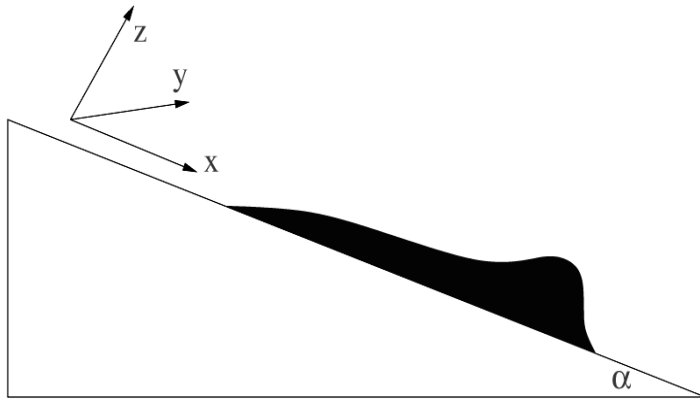


Fig. 2 Sketch of the fluid in two-dimensional geometry. The capillary ridge, which forms just behind the fluid front, can easily be seen in experiments as a drop that forms as the fluid flows down an incline. In most of this work we will neglect thinning of the fluid far behind the front.

an initial fluid shape. BCs are more involved, since they reflect the interaction of the fluid film with the solid, and also with the air at the free surface (see Figure 2). At the fluid–solid interface, one usually uses the so-called no-slip BC, that specifies that

the tangential component of the fluid velocity vanishes there [2]. The BC at the free surface is that there is a jump of pressure across the interface. The size of this jump is proportional to surface tension. This is a material parameter that is responsible, e.g., for keeping liquid drops together; essentially it tends to decrease the surface to volume ratio. If the interface is flat, the jump in the pressure is zero. If the interface is curved, this jump is a linear function of the curvature, κ , of the free surface [2].

2.1. Reduction of Navier–Stokes to Thin Film Equations. Equations (2), combined with the outlined BCs, are very complicated and difficult to address by either analytical or numerical means. There is, however, one property of all thin film flows that can be used for significant simplification. The film is thin; hence, the ratio of the film thickness, h , and any in-plane length-scale, L , becomes a small parameter, ϵ . In Appendix A we show how the smallness of ϵ simplifies the formulation. In particular, by averaging over the fluid thickness, we effectively reduce the number of relevant spatial dimensions. This helps tremendously in both theoretical and computational analysis.

The reduction of N–S equations (often called lubrication, or long-wave approximation) leads to the following PDE for the fluid thickness, $h(x, y, t)$ (see Appendix A),

$$(3) \quad \frac{\partial h}{\partial t} = -\frac{1}{3\mu} \nabla \cdot [\gamma h^3 \nabla \nabla^2 h - \rho g h^3 \nabla h \cos \alpha + \rho g h^3 \sin \alpha \mathbf{i}],$$

where now $\nabla = (\partial_x, \partial_y)$. The fourth-order term results from surface tension (which tends to flatten the free surface), and the last two terms are due to gravity. Note that (3) is strongly nonlinear, requiring care in finding the solution(s) and understanding of their properties.

Considering only the highest order term, (3) is a fourth-order diffusion equation and has a number of interesting properties. One of them is the lack of maximum principle, satisfied by the (usual) second-order diffusion. A consequence is that the solutions of (3) are not bounded from either above or below. Therefore, even if the initial condition is nonzero everywhere (i.e., the fluid completely covers the domain), there is no guarantee that a solution will satisfy this property for all times. Closer inspection of (3) reveals also that it is degenerate, meaning that the coefficient of the highest order terms (h^3) vanishes as $h \rightarrow 0$. This and other properties of the equations such as (3) are outlined in accessible manner in [4]. An alternative derivation of the lubrication approximation, as well as an overview of a variety of problems involving thin films, can be found in [14].

2.2. Nondimensionalization and Basic Properties of Thin Film Equations.

The first step in solving (3) is to put it in a nondimensional form. To do this, we scale the fluid height, h , by the thickness far behind the front, h_c . Next, we rescale the in-plane coordinates, and time, by defining $(\bar{x}, \bar{y}, \bar{t}) = (x/x_c, y/x_c, t/t_c)$. Balancing the capillary (surface tension) term with the gravity ones specifies the appropriate choice for x_c . The requirement that the time derivative term is of the same order as the terms on the right-hand side (RHS) of (3) yields the time scale, t_c :

$$(4) \quad x_c = \left(\frac{a^2 h_c}{\sin \alpha} \right)^{1/3}, \quad t_c = \frac{3\mu}{\gamma} \frac{a^2 x_c}{h_c^2 \sin \alpha}.$$

The quantity $a = \sqrt{\gamma/\rho g}$ is called the capillary length; this is the length-scale at which the capillary effects become important relative to gravitational ones. The velocity

scale is chosen naturally as $U = x_c/t_c$. It is also appropriate to define the capillary number $Ca = \mu U/\gamma$; this quantity measures the importance of the viscous forces relative to those resulting from surface tension. Using this nondimensionalization, we obtain that (3), for $\bar{h} = h/h_c$, is given by (dropping the bars)

$$(5) \quad \frac{\partial h}{\partial t} = -\nabla \cdot [h^3 \nabla \nabla^2 h] + D(\alpha) \nabla \cdot [h^3 \nabla h] - \frac{\partial h^3}{\partial x} ,$$

where the single dimensionless parameter $D(\alpha) = (3Ca)^{1/3} \cot(\alpha)$ measures the size of the normal component of gravity.

It should be noted that the lubrication approximation requires not only that the direction normal to the plane be much shorter than any in-plane dimension, but also that the slope of the free surface be small. The reader may want to check that this requirement leads to $[(h_c/a)\sqrt{\sin \alpha}]^{2/3} \ll 1$ (assuming slopes of $O(1)$ expressed in terms of the nondimensional quantities). Therefore, the maximum thickness of the film that still satisfies the assumptions of lubrication approximation depends on α ; for small α 's, this condition is always fulfilled; however, for large α 's, it is valid only for very thin films. By specifying the parameters defining the fluid, it is easy to determine whether lubrication approximation is appropriate for a given h_c . Furthermore, after we obtain a solution of (5), we need to check that the gradients of the solution are not too large (see Exercise 2.2).

Before we proceed any further, we need to clarify one more point. There is an obvious contradiction between the use of a no-slip boundary condition that requires the parallel component of fluid velocity at the fluid–solid interface to vanish, and the motion of the fluid front. In the literature this is called “contact line paradox.” Although one can find a number of ways (some outlined below) around this issue, it is worth emphasizing that this problem is not yet resolved; i.e., the fluid behavior close to the contact line is not completely understood. Some of the possible approaches are (i) inclusion of intermolecular (van der Waals) forces explicitly into the governing equations, (ii) allowing for a fluid to slip at the boundary, or (iii) assuming that the surface is already prewetted by a very thin fluid layer, called precursor film. This last approach (used in this paper) is appropriate even when the surface itself is dry but the fluid is completely wetting, such as silicon oil spreading on glass shown in Figure 1. The interested reader can find a more complete description of the contact line problem in, e.g., [7] and the references therein; in particular, [8] provides a detailed overview of this issue.

2.3. Two-Dimensional Equation and Traveling Waves. Equation (5) is much simpler than the original N–S formulation (2). However, it is still a strongly nonlinear PDE. To gain basic understanding of some of its solutions, it is useful to simplify it even further. One simplification is to assume that h is y -independent, meaning that the film flows without developing any structure in the transverse direction. This assumption reduces (5) to the following PDE with one space variable:

$$(6) \quad \frac{\partial h}{\partial t} = -[h^3 h_{xxx}]_x + D(\alpha) [h^3 h_x]_x - (h^3)_x .$$

One possible choice for the BCs is

$$(7) \quad h(0, t) = 1, \quad h(L_x, t) = b, \quad h_x(0, t) = h_x(L_x, t) = 0 ,$$

where L_x is the domain size and b is the precursor film thickness, $b \ll 1$. The idea behind (7) is that both far behind and far in front of the contact line, h does not change

(the fluid is flat) and the thickness is fixed. This assumption is not exactly satisfied whenever we have a fixed volume of fluid spreading, since the film thins with time. However, both experiments and theory show that this thinning typically happens on a much longer time scale than the development of instability (see Appendix D). Correspondingly, it is a reasonably good approximation to assume that h is fixed at $x = 0, L_x$. These BCs lead to a traveling wave solution for $h(x, t)$. That is, one can define a function $h_0(\xi) = h(x, t)$, where $\xi = x - Ut$, that satisfies (6) and the BCs (7). Plug $h_0(\xi)$ into (6) and integrate once to obtain this ODE:

$$(8) \quad -Uh_0 + h_0^3 h_{0\xi\xi\xi} - D(\alpha)h_0^3 h_{0\xi} + h_0^3 = d.$$

The BCs (7) yield $d = -b(1+b)$, $U = 1 + b + b^2$. In the limit $b \rightarrow 0$ we obtain $U \rightarrow 1$, independently of α ; this is one of the reasons for choosing the scaling (4). One can think of (8) as an equation for the fluid profile in the reference frame moving with velocity U down an incline; in that frame the fluid profile does not change with time.

To summarize, we have significantly simplified the problem from a system of nonlinear PDEs (2) to a single ODE (8). This ODE is, of course, not sufficient to completely understand the instability problem we are set to explore; it is, however, a very good starting point. This equation can be solved numerically using, i.e., the nonlinear shooting method. However, it turns out that it is actually easier to solve the PDE (6) directly. The numerical solution of that equation is outlined below.

2.3.1. Numerical Results. The computational codes needed for efficient and accurate solutions of high-order PDEs in more than one space dimension (such as (5)) are often very elaborate. However, simple equations of the form (6) are relatively easy to solve. Appendix B presents the details of an appropriate numerical procedure; some results are given below. Use of commercial software, such as MATLAB, may be also appropriate.

Figure 3 shows the evolution of the fluid profile where the initial condition is a smooth curve connecting two flat regions via a transitional part about the initial front position, chosen at $x_f = 5$. The results that follow are independent of L_x , or of the details of the initial condition. The snapshots of the fluid profiles show that, after initial transients, the flow develops a traveling wave profile, as outlined above, traveling with the speed equal to $v_f = 1 + b + b^2$. Note that computations can also be performed in the traveling frame, moving with v_f (i.e., in terms of the ξ coordinate instead of x). In that frame, the film profile is steady after initial transients.

The main feature of the profile $h(x, t)$ is the presence of a bump (capillary ridge) near the contact line. This bump is much larger for $D = 0$, shown in Figure 3a, than for $D = 1$, Figure 3b. In what follows, we will see that the height of the bump is important in order to understand the stability of the flow with respect to perturbations in the transverse direction. This bump can be seen by the naked eye in the physical experiments outlined in section 3 (or simply by observing the flow of paint down a wall).

Remark. In experiments, the BCs are typically slightly different, since there is a fixed volume of the fluid supplied, and therefore the BC $h(0) = 1$ is not satisfied. The numerical simulation can be easily modified to account for this difference by replacing $h(0) = 1$ with $h_{xxx}(0) = 0$. The resulting profile can then be compared to the similarity solution outlined in Appendix D.

2.4. Three-Dimensional Flow and Linear Stability Analysis. The main question that we want to answer is whether the contact line is stable (straight) or not.

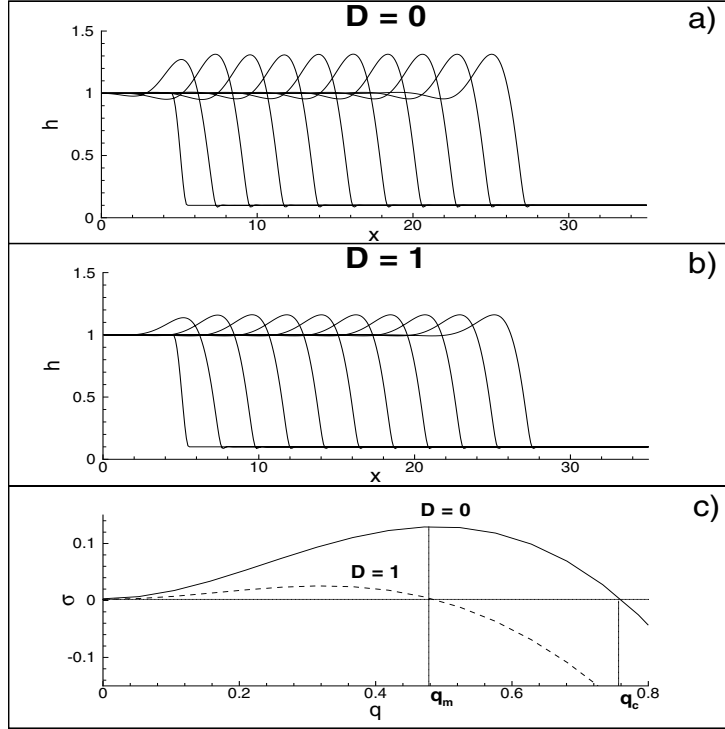


Fig. 3 Parts (a) and (b) show snapshots of the fluid profile at $\delta t = 2$ intervals, obtained as a numerical solution of (6), using $L_x = 40$, $b = 0.1$, and $\Delta x = 0.05$; the computational method is outlined in Appendix B. Part (c) shows the results of linear stability analysis (34) (see section 2.4 and Appendix C). Here, $q = 2\pi/\lambda$ is the wavenumber and σ is the growth rate of a small disturbance. The mode of the maximum growth, q_m , is the one expected to appear in physical experiments and should be compared to the distance between the patterns; see Figure 1 and Table 1.

If not, can we understand the mechanism which governs the characteristics of the emerging patterns, such as their growth, or the distance between them? In order to reach the answers, it is necessary to include the third, transverse, direction.

Before proceeding to three-dimensional (3D) geometry, it is useful to recall the typical experimental results (see section 3). After the fluid is released, for some time it flows down uniformly, without developing any structure in the y direction (see Figure 1a). During this initial time period, the solution of (8) (or, equivalently, of (6)), describes realistically the dynamics of the fluid film. For longer times, patterns start growing on top of this “base” solution. This scenario suggests that some insight into instability can be obtained by superimposing a small perturbation on the base solution, and following its time evolution. More precisely, consider (5) in the moving frame defined by (ξ, y) , and assume a solution in the form

$$(9) \quad h(\xi, y, t) = h_0(\xi) + \epsilon h_1(\xi, y, t),$$

where $\epsilon \ll 1$ and h_1 (in some norm) is of $O(1)$. Next, plug this ansatz into (5) and keep only terms to $O(\epsilon)$. This approach reduces the original problem (5) to a *linear* problem for the correction, h_1 . Since linear problems are much easier to solve, we expect to obtain h_1 with less effort than the full solution, h . The time evolution of

h_1 will give us some insight into the initial development of instability. If h_1 becomes large, this approach is no longer valid, since ϵh_1 could become comparable to h_0 . The full derivation of the equation for the correction, h_1 , is given in Appendix C.

To simplify the problem, use the fact that the y -dependence of the solution, $h_1(\xi, y, t)$, can be expressed as a continuous superposition of Fourier modes,

$$(10) \quad h_1(\xi, y, t) = \int_{-\infty}^0 g(\xi, t) e^{iqy} dq .$$

Here q is a wavenumber, which is related to the spatial period of the perturbation, λ , by $q = 2\pi/\lambda$. For convenience, consider a semi-infinite domain, $-\infty \leq \xi \leq 0$. The function g satisfies the *linear* equation (34), given in Appendix C (for simplicity of notation, the dependence of g (and of σ below) on q is not stated). The next step is to realize that the explicit time dependence of g has to be exponential due to the fact that it satisfies the homogeneous equation (34). Hence

$$(11) \quad g(\xi, t) = \phi(\xi) e^{\sigma t} .$$

The quantity σ , called the growth rate, determines the time evolution: if σ is positive, any small perturbation (possibly due to microscopic noise) grows and develops patterns; if σ is negative, a perturbation disappears.

Equation (34), while linear, involves the solution, h_0 , of the base problem (8), which is not known analytically. Then (34) has to be solved numerically as well. Some insight, however, can be reached without resorting to numerics.

Let us consider the limit of small q , i.e., of very long wavelengths. Simple but rather tedious computation shows (see Appendix C) that, for small q (and letting $b \rightarrow 0$),

$$(12) \quad \sigma(q) \approx q^2 \int_{-\infty}^0 h_0(h_0^2 - 1) d\xi .$$

For larger q 's, there is an additional term proportional to q^4 . That term produces a negative contribution to $\sigma(q)$, since it involves surface tension, which always stabilizes short wavelengths. Therefore, the only possibility for σ to be positive is if the integrand in (12) is positive. Hence, h_0 has to be larger than 1 for a considerable part of the domain if the flow is to be unstable.

Now we can understand why the capillary ridge of the solution is important. According to the just presented results, only the fluid film that develops a sufficiently large capillary ridge can become unstable. Therefore, if we can solve the two-dimensional (2D) problem and obtain h_0 , we can then calculate the integral, (12), and obtain σ . This gives the answer to one of the questions, regarding stability of the flow.

What we still do not know is, if the flow is unstable, how to determine the distance between the emerging patterns. To answer that question, we need to determine $\sigma(q)$ for all q 's. There are many ways to achieve this goal. One of them is to solve the linear PDE (34); an alternative is to use (11) to formulate (and solve) an eigenvalue problem for $\phi(\xi)$ (see Appendix C). The results presented here are obtained using the first approach (see Appendix C.2); the second method is explained in some detail in [17].

Figure 3c is typical: for small q 's, the resulting σ is positive, but for large q 's, it is always negative. Within the band of unstable modes, there are some q 's which are

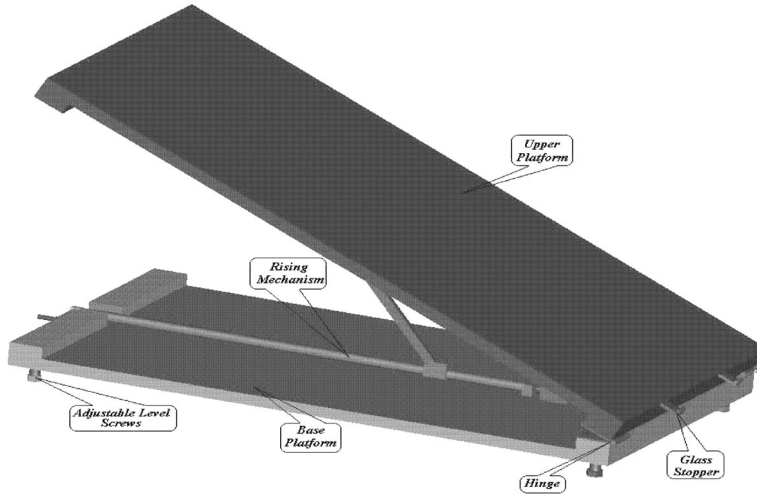


Fig. 4 Plan of the apparatus used in the experiments. The glass is fixed to the upper platform, and the rising mechanism allows for easy change of the inclination angle.

characterized by the largest growth rates (about $q \approx 0.5$ in Figure 3c). Recalling now that large positive σ implies exponential growth with time, we immediately conclude that these modes are the ones that grow in physical experiments. Hence, we can proceed to make a meaningful comparison between theoretical, computational, and experimental results, and test the validity of our theory.

The procedure outlined here is called linear stability analysis (LSA). It is very commonly used in a variety of problems. Its most important aspect is that it reduces nonlinear problems to linear ones and allows for the use of the superposition principle and other methods appropriate to linear problems. This approach is valid as long as the size of the perturbation is $O(1)$, as assumed above; if the perturbation itself is large, then LSA is not valid any more. In that case, one needs to resort to full numerical solution of the corresponding nonlinear problem. However, even in that case, the results of LSA are indispensable for the purpose of verifying the computational results.

Exercise 2.1. Use (3) and the definition of scales, (4), to derive the nondimensional thin film equation, (5).

Exercise 2.2. Recall that the lubrication approximation requires that the gradients of the solution be small. Estimate the maximum gradients shown in Figures 3a and 3b, and find the relation between the *dimensional* fluid variables and the angle α necessary for the lubrication approximation to hold (see also the discussion in section 2.1 and Appendix A).

3. Experimental Techniques. Immediate comparison of theoretical and experimental results is a very attractive feature of the presented problem. In this section, we will first overview the experimental apparatus, and then review the data acquisition techniques and the comparison to theoretical results.

3.1. Experimental Apparatus. Figure 4 shows a simple setup which is used at NJIT. It consists of a wooden frame of dimensions of 100×50 cm, arranged in such a way that the angle of the plane can easily be modified. A piece of glass of the same dimension as the frame is attached, and the fluid is released close to the top of the

plane using a simple mechanical “dam” consisting of a piece of rubber fixed to a metal frame. After the release, the fluid flow is recorded using a digital camcorder. The movie is then stored on a computer and later used for data analysis.

The fluid itself is polydimethylsiloxane (PDMS) (AlfaAesar Ward Hill, MA), also known as silicon oil (viscosity: 50 cSt; surface tension: 21 dyn/cm; density: 0.96 g/cm³). The fluid is cleaned off after an experiment is performed using soap and water. The goal of the cleaning is not to take off the oil, but to achieve a reproducible experimental environment by removing macroscopic sources of noise, such as pieces of dust. Typically, 25 grams of PDMS are used per experiment. I note that a squeegee is useful for demonstration purposes; one can use it to push the fluid up, and let it flow down again.

Before proceeding with data analysis, it should be noted that experiments can be performed using other, commonly available fluids such as vegetable oil or glycerin, or using other surfaces, such as plexiglas. Different fluid/solid combinations, however, have different wetting properties, which are known to influence the shape of the emerging patterns (see, e.g., [11]). The issue of the pattern shape is, however, complicated by the fact that the inclination angle also influences the shape, as can easily be verified in experiments; see also [1] for computational results. On a more relaxed note, readers can perform a simple experiment in their free time by gently shaking some red wine in a glass. A rim forms above the surface, which then becomes unstable in a similar manner to the flow analyzed here. Interestingly enough, this setup leads to a secondary instability of evaporative origins; details can be found in [9] and the references therein.

3.2. Data Analysis and Comparison to Theoretical Results. There are a number of experimental results that can be measured and compared to theoretical ones. The most obvious one is the distance between the developing patterns (see Figure 1), which should be comparable to the wavelength of maximum growth obtained from LSA (see Figure 3c), when expressed in terms of physical units. Careful inspection of (4) shows that the needed scales involve the unknown film thickness far behind the contact line, h_c (the other quantities are material parameters). We recall that the theoretical analysis assumes constant thickness of the fluid, while in the experiments the fluid thins far behind the front. One common approximation is to use the fluid thickness at the time when instability first starts developing. To determine this quantity, assume for a moment that the fluid of volume V is of rectangular solid shape characterized by width, W , length, x_f , and thickness, h_c . Take $W = 50$ cm, and approximate the distance the fluid spreads before it becomes unstable by x_f . This distance is typically about 5–10 cm, depending on the value of α . Then, $h_c = V/(Wx_f) \approx 0.5 - 1$ mm. A more precise approach is outlined in Appendix D, where the approximate shape of the fluid before the onset of instability is derived. That approach gives $h_c = 3V/(2Wx_f)$, which is the value used to determine the scales in what follows.

Table 1 shows the experimental and theoretical/computational distances between the patterns. The theoretical results are obtained from the plots similar to Figure 3c calculated for different α 's. We see that the experimental and theoretical results follow the same trend as α is changed, although there is a relatively large scatter of the results. Exercise 3.1 mentions some sources of error.

Figure 5 shows the lengths of typical patterns, obtained from the experimental movies. First, still photos (such as those shown in Figure 1) are extracted. Then the positions of a few representative tips and roots are recorded at selected time intervals. This procedure is rather time consuming, and it can be avoided by using one of the

Table 1 The table shows the inclination angle α , theoretical value of the wavelength of maximum growth λ_t , corresponding experimental value λ_{exp} , the growth rate of the mode of maximum growth σ_t , and the experimentally measured σ_{exp} .

α	λ_t (cm)	λ_{exp} (cm)	σ_t (sec $^{-1}$)	σ_{exp} (sec $^{-1}$)
30°	3.7	2.7	0.2	0.16
60°	2.3	2.5	0.3	0.20
82°	1.9	1.7	0.4	0.26

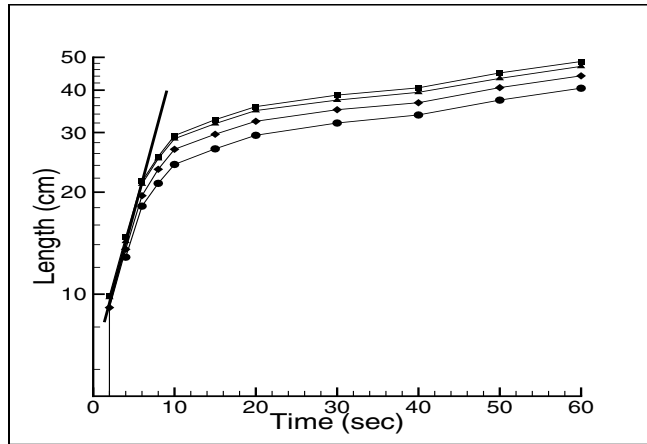


Fig. 5 Experimental results for the length of four typical patterns from Figure 1, measured from tip to root. Note that the y scale is logarithmic. The straight line is to emphasize exponential growth for early times.

available commercial software packages, if so desired. However, working directly with data provides very useful experience with movie and image analysis, extraction of information through both mechanical and automated means, and processing of large quantities of data.

Figure 5 shows that for very early times, the length versus time curve can be very well fitted by a straight line, as predicted by LSA. The slope of this line can then be compared directly to the theoretical values for the growth rate. These values, given in Table 1, are extracted from results such as those shown in Figure 3c. Similarly to the distance between the patterns, the precise comparison between theory and experiments is difficult. Both theory and experiment, however, consistently predict an increase of the growth rates as the inclination angle is increased.

For late times the growth of the pattern length is not exponential any more. In order to compare experiment and theory, we note that for long times the surface tension is relevant only in a small part of the domain (close to the fronts). Therefore, it is reasonable to ignore the surface tension altogether. This approximation allows for the formulation of an asymptotic solution, presented in Appendix D, valid for very long times. The asymptotic approach concentrates on 2D situations, hence it does not include instability and neglects the surface tension, as well as the normal component of gravity. With all these simplifications, one obtains that the position of the fluid front should vary with time according to $x_f(t) \propto t^{1/3}$.

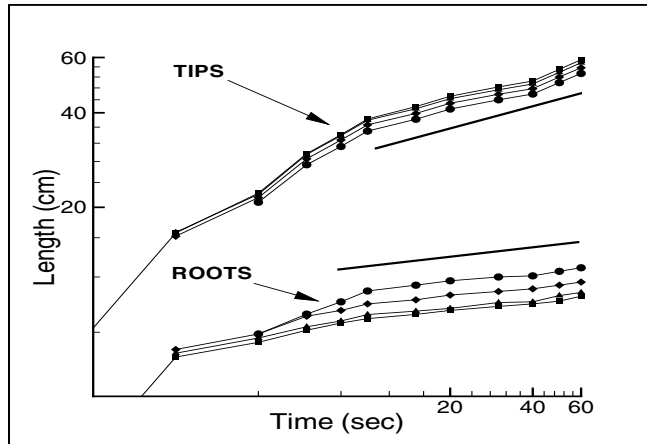


Fig. 6 Position of the tips and of the roots in the experiment shown in Figure 1. The slope of the lines can be directly related to the exponents governing the evolution for late times (see text).

Figure 6 shows the data for the positions of the tips and the roots on a log-log plot; these are the same data as in Figure 5. In order to make a comparison with experimental results, let us assume that in the experiments $x_f(t) \propto t^\beta$, and compare the value of β to $1/3$. In experiments, the fluid becomes unstable and the tips and the roots propagate according to different β 's (different slopes of the solid lines in Figure 6). In general, one expects that for the tips, β is slightly larger, and for the roots, it is slightly smaller than $1/3$. By simply estimating the slope of the experimental lines in Figure 6, one can obtain the exponents and readily verify that the prediction of the asymptotic solution is correct.

Exercise 3.1. Discuss possible sources of error responsible for the differences between theoretical and experimental results for the distance between the patterns. Consider both theoretical and experimental sources of inaccuracy. In particular, discuss the influence of the (unknown) precursor film thickness.

Exercise 3.2. Verify the degree to which the assumption $[(h_c/a)\sqrt{\sin \alpha}]^{2/3} \ll 1$ from section 2.2 is satisfied by the experimental data presented in this section. Combine your result with the estimate of the maximum slope of the solution from Figure 3 (see Exercise 2.2) to decide whether the use of lubrication approximation is justified.

4. Conclusion. At NJIT, the project outlined here was carried out during one semester by a group of six, mostly senior students. The students built the experimental apparatus and then spent some time learning how to perform the experiment and obtain reproducible results. In parallel, about three weeks were dedicated to learning the basics of fluid mechanics, as well as the reduction of N-S to the thin film equation. After this period, the students were ready to address the issues related to linear stability analysis and performed this analysis in the limit of the small wavenumber of a perturbation. The computational effort consisted of developing a C++ code that solved the governing equation (6) in two space dimensions, mostly following the approach outlined in Appendix B. My experience was that use of a (simpler) explicit method was appropriate, taking into account the computational difficulties involved in implicit schemes.

Generally, the project was very well accepted by the students. While some aspects (e.g., linear stability analysis) were rather difficult, and some other ones (e.g., the data

analysis) rather time consuming, everybody, including the instructor, was curious and interested to reach a good agreement between the experiment and the theory. Most of the work was done in groups, each of which concentrated on one aspect of the problem (theory, numerics, data analysis), with everybody participating in performing the experiment. These groups were encouraged to communicate and discuss their results, with the main goal for all of them being to develop a complete picture of the problem. At the end of the semester, the students presented their results at a public seminar, and also submitted a joint report [1].

Appendix A. Lubrication Approximation. Let us start from the N–S equations (2). Denote the fluid velocity as $\mathbf{u} = (\mathbf{v}, w)$, where w stands for the z component and \mathbf{v} for the in-plane components. Define L and h_c as the $x - y$ and z direction length-scales, respectively. Also, use U as a velocity scale (to be specified later), and let the time scale be defined by L/U . Next, define the Reynolds number which measures the relative importance of the inertial forces (left-hand side of (2)) and the viscous forces by $Re = UL\rho/\mu$. It is easy to show that if $Re \ll 1$, then the inertial terms can be ignored. Later we will need to verify that this assumption holds.

Next, define $\epsilon = h_c/L$, and $\bar{x} = x/L$, $\bar{y} = y/L$, $\bar{z} = z/h_c$. The second derivatives of the in-plane velocity components are rewritten as

$$\frac{\partial^2 |\mathbf{v}|}{\partial x^2} \approx \frac{\partial^2 |\mathbf{v}|}{\partial y^2} = \frac{1}{L^2} \frac{\partial^2 |\mathbf{v}|}{\partial \bar{y}^2} \ll \frac{\partial^2 |\mathbf{v}|}{\partial z^2} = \frac{1}{h_c^2} \frac{\partial^2 |\mathbf{v}|}{\partial \bar{z}^2},$$

where \ll holds since $h_c \ll L$. Therefore, the in-plane derivatives can be ignored. Next, based on the incompressibility relation, $\nabla \cdot \mathbf{u} = 0$, we can also safely neglect the normal component of velocity, $w \ll |\mathbf{v}|$. These simplifications reduce (2) to

$$(13) \quad \nabla_2 p = \mu \frac{\partial^2 \mathbf{v}}{\partial z^2} + \rho g \sin \alpha \mathbf{i},$$

$$(14) \quad \frac{\partial p}{\partial z} = -\rho g \cos \alpha,$$

where $\nabla_2 = (\partial_x, \partial_y)$. The last equation can be trivially integrated, and p calculated up to some function of (x, y) . This function follows from the so-called Laplace–Young boundary condition, which states that at the interface, $z = h(x, y)$, the pressure is $p(h) = -\gamma\kappa + p_0$, where κ is the curvature of the boundary, γ is the surface tension, and p_0 is the atmospheric pressure in the air phase. We obtain

$$(15) \quad p = -\rho g(z - h) \cos \alpha - \gamma\kappa + p_0.$$

Next, integrate (13) twice with respect to z , and use (15). Define $P = \rho g h \cos \alpha - \gamma\kappa$ to obtain

$$(16) \quad \mathbf{v} = \frac{1}{\mu} \nabla_2 P \frac{z^2}{2} + \mathbf{A}z + \mathbf{B} - \frac{\rho g}{\mu} \sin \alpha \frac{z^2}{2} \mathbf{i},$$

where \mathbf{A} and \mathbf{B} are vector constants.

To proceed, we need BCs. At $z = 0$, specify the no-slip BC, $|\mathbf{v}| = 0$, yielding $\mathbf{B} = 0$. At the fluid–air boundary, $z = h(x, y)$, the requirement that stresses are continuous leads to $\partial \mathbf{v} / \partial z|_{z=h(x,y)} = 0$ (since the air phase is assumed to be inviscid [2]). This condition allows us to calculate \mathbf{A} , reducing (16) to

$$(17) \quad \mathbf{v} = \left[\frac{1}{\mu} \nabla_2 P - \frac{\rho g}{\mu} \sin \alpha \mathbf{i} \right] \left[\frac{z^2}{2} - hz \right].$$

The next step is crucial. Average over the short direction to remove the z -dependence of \mathbf{v} , which would be difficult to measure anyway. Define this average by

$$(18) \quad \langle \mathbf{v} \rangle = \frac{1}{h} \int_0^h \mathbf{v} dz = -\frac{h^2}{3\mu} (\nabla_2 P - \rho g \sin \alpha \mathbf{i}) ,$$

where (17) is used. From this point on, write ∇ for ∇_2 . Conservation of mass requires

$$(19) \quad \frac{\partial h}{\partial t} + \nabla \cdot (h\mathbf{v}) = 0 .$$

Instead of the \mathbf{v} in (19), use $\langle \mathbf{v} \rangle$. Also recall the definition of P , and approximate the curvature $\kappa \approx \nabla^2 h$ (see Exercise A.2). The resulting form of (19) is

$$(20) \quad \frac{\partial h}{\partial t} = \frac{1}{3\mu} \nabla \cdot [h^3 (\rho g \cos \alpha \nabla h - \gamma \nabla \kappa - \rho g \sin \alpha \mathbf{i})] .$$

This is the so-called thin film equation (also given in section 2) that is used instead of the N-S equations to analyze the behavior of thin fluid films.

Exercise A.1. Show that the Reynolds number is indeed a small quantity. Use the definition of scales (4) to obtain U , the typical experimental distance between patterns to estimate L (see Figure 1), and the fluid parameters as given in section 3.

Exercise A.2. Derive the exact expression for the surface curvature. Find the conditions under which the approximation $\kappa \approx \nabla^2 h$ holds.

Appendix B. Numerical Methods. In order to obtain complete solution of the governing equations, one has to resort to numerical techniques. In this appendix, I outline a finite-difference-based computational technique that can be used to solve the base problem (6). Some directions for solving the more complicated linearized problem (34) are given later in Appendix C.2. The full 3D problem can be approached by similar computational techniques as well; the interested reader can find some details in [12], plots and animations in [1], and a general introduction to numerical methods for PDEs in, e.g., [13].

B.1. Space Discretization. The computational domain is defined by $0 \leq x \leq L_x$, and discretized by the node points $x_i = i\Delta x$, $i = 0, \dots, N_x$, where $\Delta x = L_x/N_x$. Let $y_i(t)$ denote a discrete approximation to $h(x_i, t)$, specified by (6). We need to formulate ODEs for dy_i/dt at each i . These equations can be written in the form

$$(21) \quad \frac{dy_i}{dt} = f_i, \quad i = 1, \dots, N_x - 1 ,$$

where f_i is a discretization of the RHS of (6). The BCs give $y_0 = 1$, $y_{N_x} = b$.

The values of f_i involve y_j at the grid points adjacent to the point i and depend on how we calculate the required derivatives. Special care is needed due to the high order of the governing equation. It is easy to check that a naive use of, e.g., central differences can lead to a large computational stencil (i.e., there would be many neighbor points involved in calculating f at a given node i). The reader can easily check that the fourth-order term would lead to a seven-point stencil, with $j = i - 3, i - 2, i - 1, i, i + 1, i + 2, i + 3$ involved (see Exercise B.1). Below I present a simpler discretization, involving only five points, but still second-order correct. Using a smaller stencil is important not only due to computational simplicity and performance, but also since a larger stencil would involve a number of extra points at the boundaries.

B.1.1. Discretization of the Fourth-Order Term. Consider the general equation

$$(22) \quad h_t = (g(h)h_{xxx})_x ;$$

in our case $g(h) = h^3$. Define forward and backward differences by

$$(23) \quad y_{x,i} = \frac{y_{i+1} - y_i}{\Delta x}, \quad y_{\bar{x},i} = \frac{y_i - y_{i-1}}{\Delta x} .$$

Equation (22) can be now discretized as

$$(24) \quad y_{i,t} = (a(y_{i-1}, y_i) y_{\bar{x}x\bar{x},i})_x ,$$

where $a(s_1, s_2)$ is some approximation to $g(h)$. It can easily be verified that (i) this scheme leads to a five-point stencil; i.e., two neighbor points on each side of the given point i are used; and (ii) the scheme is second-order correct, as long as a is a second-order correct approximation to g . The only remaining question is the choice of a . One could use, for example,

$$(25) \quad a(s_1, s_2) = \frac{1}{2} [g(s_1) + g(s_2)] \quad \text{or} \quad a(s_1, s_2) = g\left[\frac{1}{2}(s_1 + s_2)\right] .$$

Remark. Some recent works have shown that there are particular a 's that have some special properties. For example, there is a choice that leads to the so-called positivity-preserving scheme, meaning that if one starts from strictly positive data for h , the scheme will help preserving this property. The interested reader is referred to [4] and the references therein concerning the details.

B.1.2. Discretization of Lower Order Terms. The performance of a scheme is usually determined by the discretization of the highest order term, so that discretization of the lower order terms is not so important, as long as it is second-order correct. The reader may want to experiment with different kinds of discretizations and compare the convergence properties of the resulting schemes. One simple possibility is to discretize the second term in the RHS of (6) as

$$(26) \quad \left(\frac{\partial}{\partial x} h^3 h_x \right)_i \approx \frac{1}{(\Delta x)^2} (a(y_{i+1}, y_i) y_{x,i})_{\bar{x}} ,$$

while the last term can be discretized as

$$(27) \quad \left(\frac{\partial h^3}{\partial x} \right)_i \approx \frac{1}{2\Delta x} (y_{i+1}^3 - y_{i-1}^3) .$$

B.2. Time Discretization. There are different schemes that can be used to solve the system of coupled ODEs (21). The simpler ones are explicit schemes, which use the values of f_i in (21) at time t to calculate the time derivative. The simplest possibility is the forward Euler scheme, where one discretizes as

$$(28) \quad \frac{y_i(t + \Delta t) - y_i(t)}{\Delta t} = f_i(t) , \quad i = 1, \dots, N_x - 1 ,$$

and then solves this system of equations for $y_i(t + \Delta t)$, $i = 1, \dots, N_x - 1$.

This scheme, while simplest to use, suffers from two problems. One is lack of accuracy; as one could easily check, it is only first order in time. This problem can

be removed by using more accurate schemes, such as second- or fourth-order Runge–Kutta methods. A more problematic issue is the well-known fact that explicit schemes may become unstable if a time step is too large. For (21), the stability requirement is that $\Delta t < C[\Delta x]^4$, where C is a constant (the fourth power is related to the fourth order of (6)). For reasonably small Δx , this requires rather small Δt . This issue can be remedied by using implicit schemes, outlined below.

Remark. It is worth noticing that, despite their shortcomings, explicit methods have been successfully used for the problem [1]. Therefore, it is not necessary to invoke more elaborate implicit methods for the 2D problem, which we address here. For 3D problems, on the other hand, implicit schemes are much more relevant; see [6, 12].

B.2.1. Implicit Schemes. Implicit schemes use the values of f in (21) not only at time t , but also at time $t + \Delta t$ (there are also so-called multilevel schemes that use the values from other time levels; see [13]). A rather standard method is the θ -scheme, which is formulated as follows:

$$(29) \quad \frac{y_i(t + \Delta t) - y_i(\Delta t)}{\Delta t} = \theta f_i(t) + (1 - \theta)f_i(t + \Delta t), \quad i = 1, \dots, N_x - 1,$$

where $0 \leq \theta \leq 1$. Here, $\theta = 0$ leads to the forward Euler scheme, $\theta = 1$ to the (implicit) backward Euler scheme, and $\theta = 1/2$ to the implicit second-order Crank–Nicholson scheme. Any $\theta \neq 0$ specifies a system of $N_x - 1$ *nonlinear* algebraic equations for $y_i(t + \Delta t)$, $i = 1, \dots, N_x - 1$. One commonly used approach to solving this kind of equation is a variation of Newton’s method. Basically, one linearizes (29) about a guess for the solution, and then solves the resulting *linear* system for the correction. The guess is then updated and this iterative procedure repeated until the convergence criterion is met. More precisely, the solution of (29) at time t^{n+1} is written as

$$y_i^{n+1} = y_i^* + q_i, \quad i = 1, \dots, N_x - 1,$$

where y_i^* is a guess and q_i is the correction. As a guess, one can use, e.g., the solution from the previous time step, y_i^n . To linearize the equations, we express $f_i^{n+1}(= f_i(t^{n+1}))$ using the Taylor expansion of f_i^n about y_i^* :

$$f_i^{n+1} = f_i^* + \left. \frac{\partial f_i}{\partial q_j} \right|_* q_j, \quad i = 1, \dots, N_x - 1,$$

where the superscript $*$ indicates that f_i is calculated using y_j^* . Equations (29) become

$$(30) \quad (\delta_{i,j} + \theta \Delta t F_{i,j}^*) q_j = R_i, \quad i = 1, \dots, N_x - 1,$$

where $\delta_{i,j}$ is the Kronecker delta, and $F_{i,j} = \partial f_i / \partial q_j$ is the Jacobian matrix. The RHS of this linear system is

$$R_i = y_i^n - y_i^* + \theta \Delta t f_i^* + (1 - \theta) \Delta t f_i^n, \quad i = 1, \dots, N_x - 1.$$

The correction q_i is then obtained by solving the linear algebraic system (30); this completes one Newton iteration. Next, one checks whether q_i is sufficiently small (in some norm). If yes, the procedure is finished, and $y_i^* + q_i$, $i = 1, \dots, N_x - 1$, becomes the solution at time t^{n+1} . If not, one uses $y_i^* + q_i$ as a new guess and repeats the procedure until the norm of q_i is sufficiently small. The linear system itself can be solved using any standard method, such as Gaussian elimination. Of course, use of iterative methods, such as SOR or biconjugate gradient, is appropriate as well [13].

Exercise B.1. Apply central difference formulae directly to (22), without using forward/backward difference formulae (23). Show that you obtain a seven-point formula; i.e., three points on each side of a given point (plus the point itself) are needed to calculate the fourth derivative. Then, show that the discretization defined by (24) leads to a five-point computational stencil. Next, use Taylor series to show that if a is a second-order correct approximation to g , then the scheme (24) is itself of second order.

Exercise B.2. Use (24), (26), and (27) to reduce the continuous equation (6) to its continuous time, discrete space version, (21). Write down explicitly the expressions for f in (21) that result if either of the interpolations specified by (25) is used.

Appendix C. Linear Stability Analysis (LSA). The basic ideas behind LSA are introduced in section 2. Here I provide some details; the reader should also consult [3, 5, 15, 16, 18], where this problem is presented in complementary ways, including an introduction to various concepts, such as the superposition principle, normal mode expansion, eigenvalue problems, etc. The presentation here is simplified considerably in order to concentrate only on the most relevant questions. One simplification is to let $b \rightarrow 0$. Furthermore, the origin of the coordinate system is positioned at the unperturbed contact line, and for convenience we will assume a semi-infinite $[-\infty, 0]$ domain.

In section 2, I explained the motivation for expanding the solution in the moving reference frame, traveling with velocity U . In this reference frame, we have

$$(31) \quad \frac{\partial h}{\partial t} + \nabla \cdot [h^3 \nabla \nabla^2 h] - D(\alpha) \nabla \cdot [h^3 \nabla h] + \frac{\partial h^3}{\partial \xi} - U h_\xi = 0 ,$$

where $\xi = x - Ut$ and $\nabla = (\partial_\xi, \partial_y)$. Write down a solution in the form

$$(32) \quad h(\xi, y, t) = h_0(\xi) + \epsilon h_1(\xi, y, t) ,$$

where $\epsilon \ll 1$, and substitute this expansion into (31). The leading order terms ($O(\epsilon^0)$) give the 2D equation (8). The first-order terms ($O(\epsilon^1)$) yield

$$(33) \quad \begin{aligned} \frac{\partial h_1}{\partial t} = & -\nabla \cdot [h_0^3 \nabla \nabla^2 h_1 + 3h_0^2 h_1 \nabla \nabla^2 h_0] \\ & + D(\alpha) \nabla \cdot [h_0^3 \nabla h_1 + 3h_0^2 h_1 \nabla h_0] - (h_0^2 h_1)_\xi + U h_\xi , \end{aligned}$$

where f_ξ stands for $\partial f / \partial \xi$. The next step is to replace the solution, h_1 , by its Fourier integral in y ; see (10). The superposition principle tells us that we can consider each q separately, due to linearity of (33). Therefore, for a given q , we substitute (10) into (33) to obtain the following equation for g (see Exercise C.1):

$$(34) \quad \frac{\partial g}{\partial t} = -\mathcal{L}g ,$$

where the linear operator, \mathcal{L} , is given by

$$(35) \quad \begin{aligned} \mathcal{L} = & h_0^3 \frac{d^4}{d\xi^4} + (h_0^3)_\xi \frac{d^3}{d\xi^3} - (D(\alpha) + 2q^2) h_0^3 \frac{d^2}{d\xi^2} \\ & + (2 - (h_0^3)_\xi (D(\alpha) + q^2)) \frac{d}{d\xi} + h_0^3 q^2 (D(\alpha) + q^2) . \end{aligned}$$

The homogeneity of (34) implies exponential time dependence of $g = \phi(\xi)e^{\sigma t}$ (11). The growth rate, σ , determines the temporal evolution of h_1 . Using (11), (34) can be rewritten as

$$(36) \quad \mathcal{L}\phi = -\sigma\phi .$$

The last equation is an eigenvalue problem for the linear operator \mathcal{L} ; the values of σ satisfying this equation are eigenvalues, and the corresponding ϕ 's are eigenfunctions. Since $\sigma = \sigma(q)$, the perturbations characterized by different wavelengths $\lambda = 2\pi/q$ behave differently. Figure 3c shows an example where there is a range of q 's for which σ is positive; these perturbations grow with time. Outside of this range, σ is negative, and these perturbations decay exponentially.

To obtain the results shown in Figure 3c, one needs to solve (36). In general, this can be done only numerically (see Appendix C.2). However, an analytic solution can be obtained in the limiting case of very small q 's, as explained below.

C.1. Limit of Small Wavenumber. Note that (36) contains only even powers of q , up to q^4 . Then the solution should depend only on even powers of q as well:

$$(37) \quad \phi = \phi_0 + q^2\phi_1 + q^4\phi_2 , \quad \sigma = \sigma_0 + q^2\sigma_1 + q^4\sigma_2 .$$

If q is small, the terms $O(q^4)$ are not relevant. I concentrate on this limit, and proceed to derive the equations for ϕ_0 and ϕ_1 . (Note that (36) has to be valid for all q 's. Correspondingly, each power of q can be considered separately.)

C.1.1. $O(q^0)$. Substituting expansion (37) into (36), we obtain

$$(38) \quad [2\phi_0 - D(\alpha)h_0^3\phi_{0\xi} + h_0^3\phi_{0\xi\xi\xi}]_\xi = -\sigma_0\phi_0 .$$

To proceed, consider the BC at the contact line. The perturbation, g , modifies the position of the contact line from $\xi = 0$ to $\xi = \xi_b$, where $\xi_b(y, t) = -\epsilon e^{iqy + \sigma t}$. The BC at the contact line, $h(\xi_b, y, t) = 0$, needs to be linearized:

$$(39) \quad \begin{aligned} 0 &= h(\xi_b, y, t) = h_0(\xi_b) + \epsilon h_1(0, y, t) + O(\epsilon^2) \\ &= h_0(0) - \epsilon e^{iqy + \sigma t} h_0(0)_\xi + \epsilon g(0, t) e^{iqy} + O(\epsilon^2) \\ &= \epsilon e^{iqy + \sigma t} (-h_0(0)_\xi + \phi_0(0)) + O(\epsilon^2) , \end{aligned}$$

where $h(0) = 0$ follows from $b = 0$; (11) and (32) were used. Note that we first expand the solution h itself to $O(\epsilon)$ and then calculate the base solution, h_0 , at the modified boundary. This requires the Taylor expansion of h_0 , which explains the term involving $h_{0\xi}$ above. The obvious conclusion is that $\phi_0(0) = h_{0\xi}(0)$, giving the BC for ϕ_0 . Going back to (38), we see that it is reasonable to try with $\phi_0(\xi) = h_{0\xi}(\xi)$ as a candidate for the solution. Plugging this ansatz into (38) leads to

$$(40) \quad [2h_{0\xi} - D(\alpha)h_0^3h_{0\xi\xi} + h_0^3h_{0\xi\xi\xi}]_\xi = -\sigma_0h_{0\xi} .$$

In Exercise C.2 below one shows that the term in the square brackets vanishes, leading to $\sigma_0 = 0$. Therefore, the Fourier mode characterized by the zero wavenumber (translation) is “marginally stable”; it does not evolve in time. This is a consequence of the translational invariance in the ξ direction: we can always move the film up or down the incline without changing its properties.

C.1.2. $O(q^2)$. To this order, (36) leads to the following equation that now involves ϕ_0 and ϕ_1 :

$$h_0^3 \phi_{1\xi\xi\xi\xi} + (h_0^3)_\xi \phi_{1\xi\xi\xi} - D(\alpha) h_0^3 \phi_{\xi\xi} - 2h_0^3 \phi_{0\xi\xi} + (2 - (h_0^3)_\xi D(\alpha)) \phi_{1\xi} - (h_0^3)_\xi \phi_{0\xi} + h_0^3 D(\alpha) \phi_0 = -\sigma_1 \phi_0 .$$

Simplifying this equation leads to

$$(41) \quad -h_0^3 \phi_{0\xi\xi} + [h_0^3 (\phi_{1\xi\xi\xi} - D(\alpha) \phi_{1\xi} - \phi_{0\xi})]_\xi + h_0^3 D(\alpha) \phi_0 = -\sigma_1 \phi_0 .$$

Now, integrate (41) over the domain and use $\phi_0 = h_{0\xi}$ to obtain

$$(42) \quad \int_{-\infty}^0 \sigma_1 h_{0\xi} dx = \int_{-\infty}^0 h_0^3 h_{0\xi\xi\xi} dx - D(\alpha) \int_{-\infty}^0 h_0^3 \phi_0 dx .$$

Note that the term inside the square brackets in (41) does not contribute, due to the BCs. Finally, use (8) to perform the integration in (42), yielding

$$(43) \quad \sigma_1 = \int_{-\infty}^0 h_0 (h_0^2 - 1) dx .$$

Following the same approach, one can also derive the result for nonzero b [5, 16]:

$$\sigma_1 = \frac{1}{1-b} \int_{-\infty}^0 (h_0 - 1)(h_0 - b)(h_0 + b + 1) dx .$$

C.2. LSA for Arbitrary Wavenumber. If q is not small, one needs to solve either (36) or (34) numerically and extract the growth rate for all q 's. It turns out that solving (36) is a nontrivial task; the interested reader is referred to [17]. Solving (34) is, however, easier, and the results can be obtained by the following procedure (an alternative approach can be found in [3]):

1. Obtain a discrete approximation to $h_0(\xi)$, as outlined in Appendix B. Note that Appendix B concentrates on solving (6), while here we need a solution of (8). The simplest approach is to calculate the solution of (6) for late times; that solution is steady in the moving reference frame (see Figure 3).
2. Fix q , and solve (34) (again for late times).
3. Assume that the solution depends exponentially on time (as prescribed by (11)), and extract the growth rate, $\sigma(q)$.
4. Repeat for other values of q ; i.e., return to step 2 above.

Exercise C.1. Derive (34). Note that for a given q , integral (10) reduces to ge^{iqy} . Each y derivative in (33) then produces a factor of q .

Exercise C.2. Using the original ODE, (8), and its derivative, show that the term inside the square brackets of (40) identically vanishes.

Appendix D. Self-Similar Solution. Let us concentrate on (6), applied to the flow down a vertical plane. Throughout this work, I have assumed that the fluid thickness is constant far behind the front. This assumption is, of course, only approximately correct, since the fluid eventually thins out there. In this appendix, I apply a technique, called the similarity method, to explore how this thinning process evolves in time [10]. This approach is quite general, and a very powerful method for reducing PDEs to ODEs.

First, note that far behind the front, surface tension is not important and can be safely ignored (since h_{xxx} is small). Therefore, in that region, (6) reduces to

$$(44) \quad \frac{\partial h}{\partial t} + (h^3)_x = 0 .$$

Assume a solution in the form

$$h(x, t) = h_0(t)H(\eta) ,$$

where η is our self-similar variable which measures distance to the front, $\eta = x/x_f(t)$, $0 \leq \eta \leq 1$ ($x_f(t)$ is the front position). The idea is that, after we isolate the explicit time dependence, the shape of the film will depend only on η . Before we proceed, it is to be noted that this approach does not apply close to the “real” front (contact line), since surface tension is not included.

The next step is to require that $h_0(t) = At^\alpha$, $x_f(t) = Bt^\beta$, where α, β are self-similar exponents. After simple algebraic manipulation, (44) reduces to

$$(45) \quad \frac{\dot{h}_0 x_f}{h_0 \dot{x}_f} H - \eta H' + \frac{h_0^2}{\dot{x}_f} H^2 H' = 0 ,$$

where $\dot{} = d/dt$ and $' = d/d\eta$. Now, recall that the total volume of the fluid is constant; therefore, the volume per unit width of the domain, v , is constant as well:

$$v = h_0 x_f \int_0^1 H(\eta) d\eta = \text{const.},$$

giving $\dot{h}_0 x_f = -h_0 \dot{x}_f$ and $\beta = -\alpha$. In (45), the first two terms do not depend explicitly on time; therefore, the last term shall not depend on time either, yielding $\alpha = -1/3$. Therefore, we obtain that the fluid is thinning far behind the front according to $h_0 \propto t^{-1/3}$, while the front itself propagates according to $x_f \propto t^{1/3}$.

We can now easily solve the ODE (45). Integrate it once, and use $H(0) = 0$ as a BC. The result is $H(\eta) = \sqrt{B\eta/A}$. Using (44), we obtain $A = 1/3$ and $h(x, t) = \sqrt{x/3t}$. It is now easy to show that $B = (27v^2/4)^{1/3}$. To summarize, the domain of the self-similar solution ends abruptly at

$$x_f(t) = \left(\frac{27}{4} v^2 t \right)^{1/3} ,$$

and the thickness at x_f is given by

$$h(x_f) = h_f = \left(\frac{v}{2t} \right)^{1/3} .$$

This approach allows us to determine (approximately) the fluid thickness of the plateau behind the capillary ridge (see Figure 2). Combine the last two results above to obtain that the fluid thickness at x_f is given by

$$(46) \quad h_f = \frac{3v}{2x_f} .$$

This expression is used in section 3 to estimate the scales needed to compare theoretical and experimental results. Exercise D.2 discusses under what conditions the change of the plateau thickness with time can be ignored.

Exercise D.1. By replacing the self-similar solution in the neglected terms in (6), show that it is valid if these two conditions are satisfied: $1 \ll (48x^5t)^{1/2}$, $\mathcal{D} \ll (3xt)^{1/2}$.

Exercise D.2. Compare the following two time scales: (1) $1/\sigma_M$, where σ_M is the maximum growth rate, given in Table 1, and (2) T , on which h_f specified by (46) changes significantly. Show that for the parameters as specified in section 3, $1/\sigma_M \ll T$. Based on this result, conclude that the time dependence of h_f can be safely ignored for early times of instability development.

Exercise D.3. Consider the problem of a spreading drop on a horizontal surface,

$$\frac{\partial h}{\partial t} = \frac{\partial}{\partial x} \left(h^3 \frac{\partial h}{\partial x} \right).$$

Following the similarity method, assume $h(x, t) = h_0(t)H(\eta)$, $\eta(t) = x/x_f(t)$. Use the following BCs: $H(0) = 1$, $H(1) = 0$, $H'(0) = 0$. Show that the shape of a drop is given by $(1 - \eta^2)^{1/3}$. Find how this profile evolves in time.

Acknowledgments. The author wishes to thank the group of students who performed the original experiments: Jeremy P. Carlo, Pritam O. Dodeja, Jeffrey Fernandez, Rupen Patel, Mark Timonera, and Rafal Turek (who actually built the experimental setup), and to Drs. Anna Georgieva and Greg Kriegsmann for useful comments. This paper is a byproduct of the research with Dr. Javier Diez of Universidad Nacional del Centro, Tandil, Argentina, who also helped with the original student project at NJIT.

REFERENCES

- [1] For pictures, animations, experimental results, and the student report, see http://math.njit.edu/~kondic/thin_films/thin_films.html.
- [2] D. J. ACHESON, *Elementary Fluid Dynamics*, Clarendon Press, Oxford, 2000.
- [3] A. J. BERNOFF, A. L. BERTOZZI, AND T. P. WITELSKI, *Axisymmetric surface diffusion: Dynamics and stability of self-similar pinchoff*, J. Statist. Phys., 93 (1998), pp. 725–776.
- [4] A. L. BERTOZZI, *The mathematics of moving contact lines in thin liquid films*, Notices Amer. Math. Soc., 45 (1998), pp. 689–697.
- [5] A. L. BERTOZZI AND M. P. BRENNER, *Linear stability and transient growth in driven contact lines*, Phys. Fluids, 9 (1997), pp. 530–539.
- [6] J. DIEZ AND L. KONDIC, *Contact line instabilities of thin liquid films*, Phys. Rev. Lett., 86 (2001), pp. 632–635.
- [7] J. DIEZ, L. KONDIC, AND A. L. BERTOZZI, *Global models for moving contact lines*, Phys. Rev. E, 63 (2001), pp. 011208.
- [8] E. B. DUSSAN V., *On the spreading of liquids on solid surfaces: Static and dynamic contact lines*, Ann. Rev. Fluid Mech., 11 (1979), pp. 371–400.
- [9] A. E. HOSOI AND J. W. M. BUSH, *Evaporative instabilities in climbing films*, J. Fluid. Mech., 442 (2001), pp. 217–239.
- [10] H. HUPPERT, *Flow and instability of a viscous current down a slope*, Nature, 300 (1982), pp. 427–429.
- [11] J. M. JERRETT AND J. R. DE BRUYN, *Finger instability of a gravitationally driven contact line*, Phys. Fluids A, 4 (1992), pp. 234–242.
- [12] L. KONDIC AND J. DIEZ, *Contact line instabilities of thin film flows: Constant flux configuration*, Phys. Fluids, 13 (2001), pp. 3168–3184.
- [13] K. W. MORTON AND D. F. MEYERS, *Numerical Solution of Partial Differential Equations*, Cambridge University Press, Cambridge, 1994.
- [14] T. G. MYERS, *Thin films with high surface tension*, SIAM Rev., 40 (1998), pp. 441–462.
- [15] M. A. SPAID AND G. M. HOMSY, *Stability of Newtonian and viscoelastic dynamic contact lines*, Phys. Fluids, 8 (1996), pp. 460–478.
- [16] S. M. TROIAN, E. HERBOLZHEIMER, S. A. SAFRAN, AND J. F. JOANNY, *Fingering instabilities of driven spreading films*, Europhys. Lett., 10 (1989), pp. 25–30.
- [17] E. O. TUCK AND L. W. SCHWARTZ, *A numerical and asymptotic study of some third-order ordinary differential equations relevant to draining and coating flows*, SIAM Rev., 32 (1990), pp. 453–469.
- [18] Y. YE AND H. CHANG, *A spectral theory for fingering on a prewetted plane*, Phys. Fluids, 11 (1999), pp. 2494–2515.